Characterization of Plastic Deformation Induced by Microscale Laser Shock Peening

Hongqiang Chen

Jeffrey W. Kysar

Y. Lawrence Yao

Department of Mechanical Engineering,
Columbia University,
New York, NY 10027

Electron backscatter diffraction (EBSD) is used to investigate crystal lattice rotation caused by plastic deformation during high-strain rate laser shock peening in single crystal aluminum and copper sample on $(1\bar{1}0)$ and (001) surfaces. New experimental methodologies are employed which enable measurement of the in-plane lattice rotation under approximate plane-strain conditions. Crystal lattice rotation on and below the microscale laser shock peened sample surface was measured and compared with the simulation result obtained from FEM analysis, which account for single crystal plasticity. The lattice rotation measurements directly complement measurements of residual strain/stress with X-ray micro-diffraction using synchrotron light source and it also gives an indication of the extent of the plastic deformation induced by the microscale laser shock peening.
[DOI: 10.1115/1.1782914]

1 Introduction

Shot peening is a process involving multiple and repeated impacts by bombarding a surface with relatively hard particles with sufficient velocities to indent the surface, [1]. Shot peening is widely used to improve the fatigue behavior of mechanical components by introducing compressive stress on the peened surface.

Laser shock peening (LSP) has been studied since 1960s. As shown in Fig. 1, it is a surface treatment wherein, laser-induced shocks introduce compressive residual stresses relatively deep within the material resulting in an increased resistance of the material to various forms of failure, [2]. In particular, LSP can induce compressive residual stresses in the target surface and improve its fatigue life, which is important in applications such as turbine blades of aircraft engine. The potential benefits of laser peening over shot peening include a greater residual compressive stress depth and little change to either surface finish or shape. Also the process parameters such as laser intensity and laser pulse duration are much easier to control than shot peening. Finally, it is possible to apply LSP to only selected regions of a component, because of the ability to precisely dictate the position of the laser.

Recently, laser shock processing of polycrystalline aluminum and copper using a micron length scale laser beam has been studied, [3–5]. It has been shown that microscale laser shock peening (μLSP) can efficiently induce favorable residual stress distributions in bulk metal targets as measured by X-ray diffraction with micron-level spatial resolution, [6], and calculated through finite element analysis (FEM) simulations, [7]. Thus, microscale laser shock peening (μLSP) is a technique that can be used to manipulate the residual stress distributions in metal structures over regions as small as a few microns and thus improve the reliability of microdevices.

The mechanics of laser shock peening presents many exciting challenges, because it is a hybrid process involving many disciplines. Classical solid continuum mechanics has been very successful in describing shock-compression process for conventional shot peening. However, for microscale laser shock peening, high laser power intensity (4 GW/cm^2) and short shock peening times (laser pulse duration = 50 ns) introduce high strain rate plastic deformation confined to the micron length scale. Micromechanical considerations of strain gradient plasticity, rate-dependent plasticity and its relationship to crystal structure, crystal lattice orientation, dislocation and cell structure formation under shock wave loading at the micron length scale require careful study. In addition, there is a solid-fluid interaction, because the specimen is submerged in water during the LSP process.

In this paper, electron backscatter diffraction (EBSD) is used to investigate crystal lattice rotation caused by high-strain rate microscale laser shock peening in single crystal aluminum and copper sample on $(1\bar{1}0)$ and (001) surfaces. For the first time, crystal lattice rotation on and below the microscale laser shock peened sample surface was measured; these are compared with FEM simulations based on single crystal plasticity. The experimental results provide useful insight into the high-strain rate shock peening process at the microscale. Also the experiments provide new methodologies for characterizing the microstructure formation and distribution of plastic deformation for microscale laser shock peening.

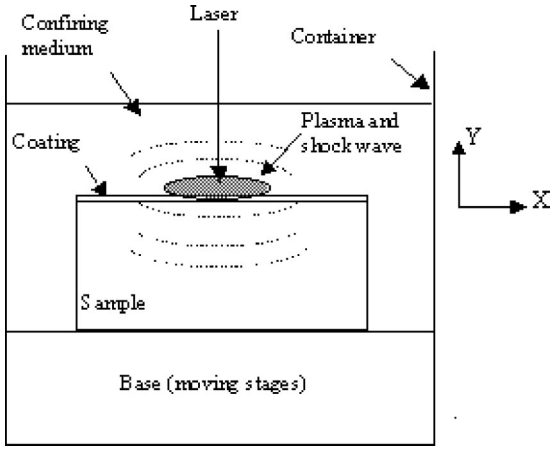

Fig. 1 Laser shock peening setup

Contributed by the Applied Mechanics Division of THE AMERICAN SOCIETY OF MECHANICAL ENGINEERS for publication in the ASME JOURNAL OF APPLIED MECHANICS. Manuscript received by the ASME Applied Mechanics Division, September 4, 2003; final revision, April 29, 2004. Associate Editor: K. M. Liechti. Discussion on the paper should be addressed to the Editor, Prof. Robert M. McMeeking, Journal of Applied Mechanics, Department of Mechanical and Environmental Engineering, University of California–Santa Barbara, Santa Barbara, CA 93106-5070, and will be accepted until four months after final publication of the paper itself in the ASME JOURNAL OF APPLIED MECHANICS.

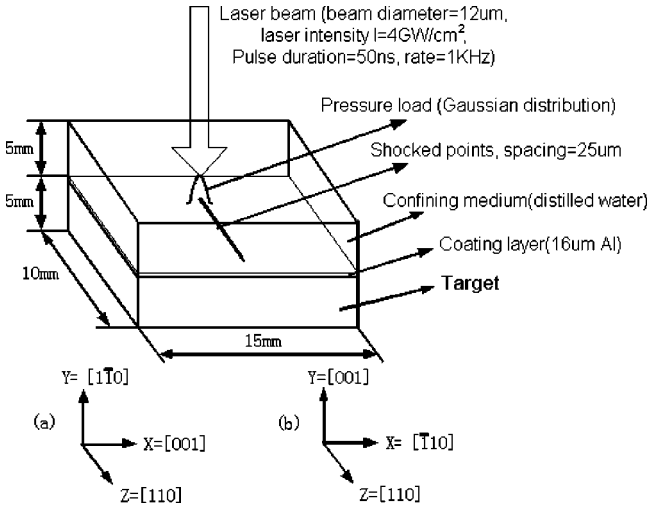

Fig. 2 Sample geometry and laser shock peening condition; (*a*) Al(1$\bar{1}$0) sample and Cu(1$\bar{1}$0) sample, (*b*) Al (001) sample

2 Material Preparation and Laser Shock Peening Conditions

Face-centered-cubic (FCC) metals such as copper and aluminum are routinely used in microdevices due to their good mechanical and electrical properties. Fully annealed single crystals of pure aluminum and copper (grown by the seeded Bridgman technique) were used for microscale laser shock peening herein. Laue X-ray diffraction was used to determine the crystal orientation within $\pm 1°$ and the sample was cut to shape using a wire electrical discharge machine (EDM). Regular mechanical polishing with diamond grit sizes 6 and 1μm was used to remove the heat affected zone of the cutting surface and electrochemical polishing was applied for all samples to eliminate any remaining deformed material prior to shock peening.

It is known that a line loading parallel to a $\langle 110 \rangle$ direction in an FCC crystal induces a state of plane deformation, [8]. Thus successive shock peens were applied to the material along a line parallel to [110] direction in an attempt to achieve a final deformation state that approximates a plane deformation state. In order to achieve a symmetric deformation field, the shock peens were applied to either the (1$\bar{1}$0) surfaces of Al and Cu or (001) surface of Al.

The samples, shown in Fig. 2, have the dimensions of 15 mm $\times$10 mm$\times$5 mm. The coordinate systems used throughout this paper are indicated in Fig. 2 and defined as follows: Z-axis is parallel to the shock line which has direction of [110], X-axis is parallel to [001] direction and Y-axis is parallel to [1$\bar{1}$0] normal to the shocked Al(1$\bar{1}$0) and Cu(1$\bar{1}$0) surfaces. For the Al (001) sample, the X-axis is parallel to [$\bar{1}$10] and Y is parallel to [001] normal of the shocked surface, with the Z-axis again parallel to the shocked line in direction of [110].

In the laser shock peening, a frequency tripled Q-switched neodymium: yttrium-aluminum-garnet (Nd:YAG) laser (wavelength 355 nm) in transverse electromagnetic modes 00 (TEM_{00}) mode was used. The pulse duration was 50 ns, spacing between consecutive pulses along a shock line was 25 μm, and pulse numbers were three on each shocked location at 1 KHz pulse repetition rate. Laser beam diameter was 12 μm and laser intensity was approximately 4 GW/cm^2. A thin layer of high vacuum grease (about 10 microns thick) was spread evenly on the polished sample surface, and a 16-μm thick polycrystalline aluminum foil, chosen for its relatively low threshold of vaporization, was tightly pressed onto the grease. The sample was placed in a shallow container filled with distilled water around 5 mm above the sample's top surface. After shock processing, the coating layer and the vacuum grease were manually removed. The induced deformation is due to shock pressure and not due to thermal effects since only the coating is vaporized by the laser shock. Further details of microscale LSP setup are given in [3–5].

3 Characterization of Laser Shock Peening

Several different experimental methods were employed to characterize the laser shock peening regions. Atomic force microscopy (AFM) was used to measure the deformation geometry on the shocked surfaces. Crystal lattice rotation was characterized by electron backscatter diffraction (EBSD) to measure crystallographic orientation as a function of position. Moreover, X-ray microdiffraction [6] was applied to measure crystal lattice rotation on the shocked surface, as well as to measure shock-induced residual stress. The result from each of these methods are discussed in detail in this section.

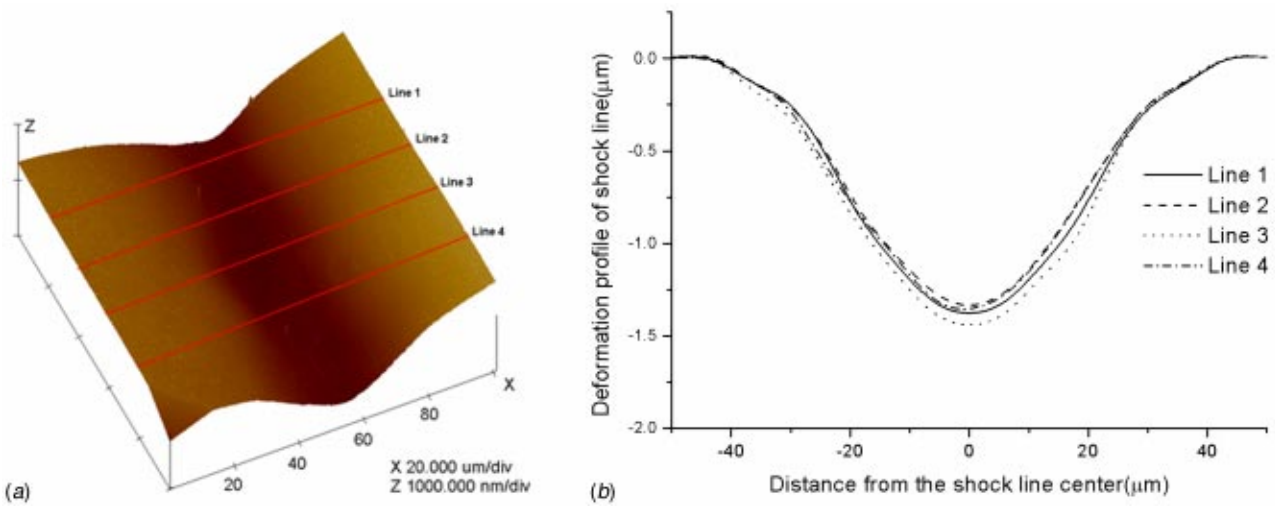

Fig. 3 Measurement of shocked line geometry using AFM for Al(1$\bar{1}$0) sample (scan area=100$\times$100 μm); (*a*) three-dimensional geometry, (*b*) cross section geometry at different positions (line spacing=20 μm)

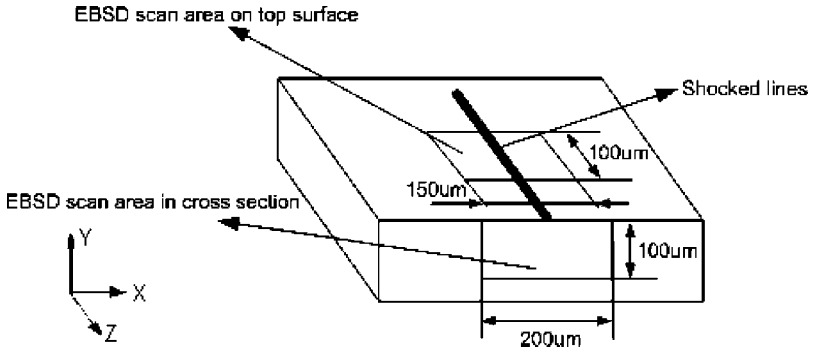

Fig. 4 EBSD automatic indexing map on top surface and on newly exposed cross section

3.1 Sample Deformation Measured by AFM. A typical three-dimensional geometry of the shocked region of Al (001) sample measured using AFM (Digital Instruments Nanoscope Inc.) is seen in Fig. 3(*a*); the scan area is 100×100 μm and 512 measurements were made along each direction. The scan direction is set to parallel to *Z*-direction (i.e., along the shock direction) to decrease the uncertainty of measurement. In order to check the deformation profiles at different location along the shocked line, detailed cross-section profiles at four different positions with spacing$=20$ μm (red lines 1–4 in Fig. 3(*a*)) are shown in Fig. 3(*b*). As is evident, the depth of the shock line is around 1.5 μm with width of 90 μm. It is clear that the shocked line is surprisingly uniform deformed along [110] direction in spite of the fact that the laser shocks were created sequentially. The lateral extent of the AFM measurements was not sufficient to show pileup on the edges of the shock line. However, additional measurement, to be discussed in Section 4.3, shows evidence of pileup.

3.2 Lattice Orientation Measurement With EBSD (Electron Backscatter Diffraction). From the work of Kysar and Briant [9], it is possible to measure the extent as well as character of the lattice rotation below the shocked surface by using electron backscatter diffraction (EBSD) to measure crystallographic orientation as a function of position. EBSD is a diffraction technique for obtaining crystallographic orientation with submicron spatial resolution from bulk samples or thin layers in a scanning electron microscope (SEM), [10].

The crystallographic orientation of the shock peened top surface was collected using EBSD, which provided information about the lattice rotation on the shocked surface. After that, in order to obtain the depth distribution and magnitude of lattice rotation below the shocked surface, the specimen was sectioned via wire EDM to expose a (110) plane in a region which experienced an approximate plane-strain deformation state due to μLSP. The newly exposed center surface was polished again after which the crystal orientation of the sectioned surface was mapped using EBSD, as indicated schematically in Fig. 4.

EBSD data was collected using a system supplied by HKL Technology, [11], and attached to a JEOL JSM 5600LV scanning electron microscope. All data were acquired in the automatic mode, using external beam scanning and employing a 1-μm step size. A typical scan area is 100 μm$\times$150 μm on the shocked surface and 200 μm$\times$100 μm on the cross section as in Fig. 4. The EBSD results from each individual scan comprise data containing the positioncoordinates and the three Euler angles which describe the orientation of the particular interaction volume of the crystal relative to the orientation of the specimen in the SEM. This information allows the in-plane and the out-of-plane lattice rotations to be calculated relative to the known undeformed crystallographic orientation, which serves as the reference state.

3.2.1 Image Pole Figure From Sample Top Surface. Pole figures or inverse pole figures are commonly used to analyze textures based on information of lattice orientation obtained from EBSD. The orientation of the crystal at each measurement position is represented by a point on the stereographic polar net, [12]. Figure 5 shows the inverse pole figure from the shocked surface for specimen Al (001) in which *Z* ([110]) is aligned with the shock line direction. The scan area covers a region ±50 μm in *X*-direction across the shocked line and 100 μm along the *Z*-direction with spatial resolution of 1 μm. It is clear from Fig. 5 that the [110] of the crystal remains closely aligned with the *Z*-axis after deformation. On the other hand, the inverse pole figures indicate a larger distribution of rotation of $[\bar{1}10]$ and [001] relative to the *X* and *Y*-axes, respectively. Thus, both the AFM and the EBSD results indicate that an approximate two-

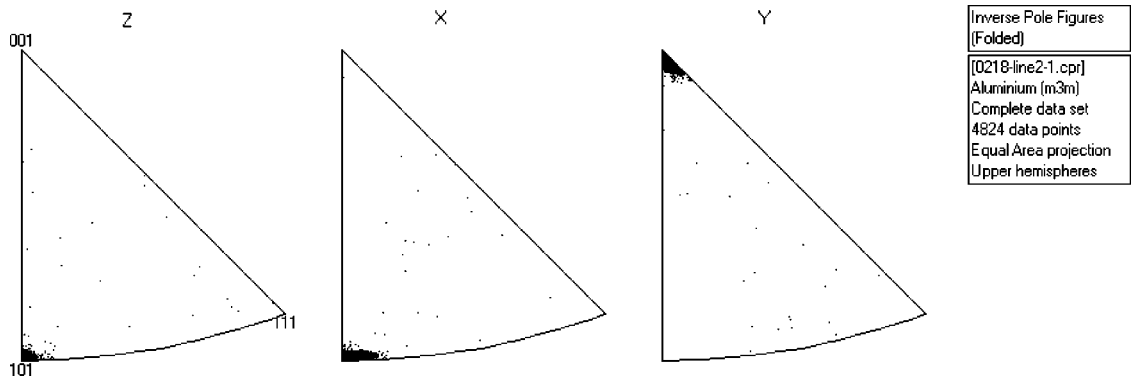

Fig. 5 Inverse pole figure of sample surface under shock peening (*Z*-direction is shock direction, *Y*-direction is the sample surface normal)

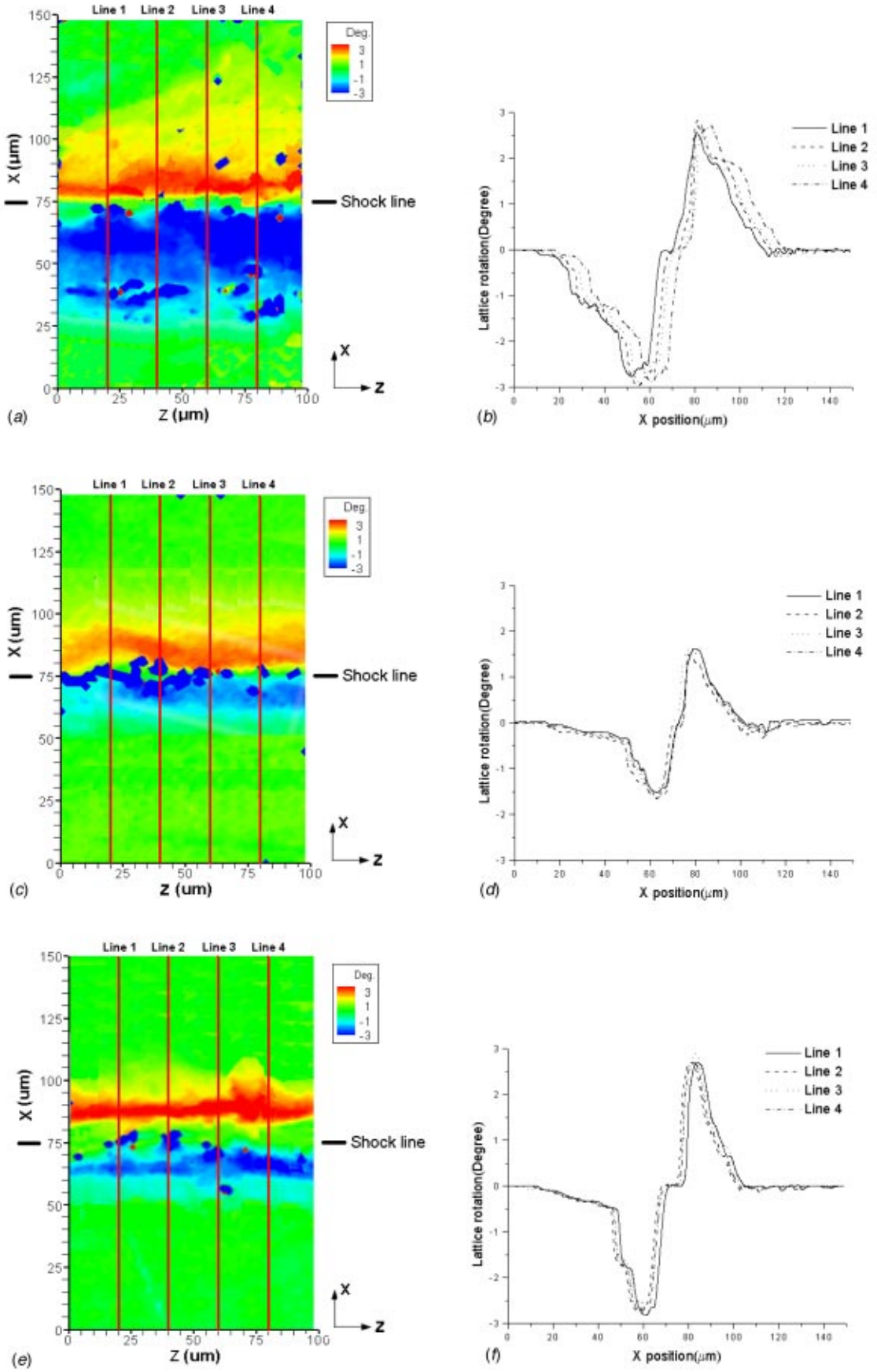

Fig. 6 Lattice rotation contour map on sample surface (line 1–4: four cross section with spacing=20 μm); (*a*) and (*b*): Al$(1\bar{1}0)$ sample; (*c*) and (*d*): Cu$(1\bar{1}0)$ sample; (*e*) and (*f*): Al (001) sample

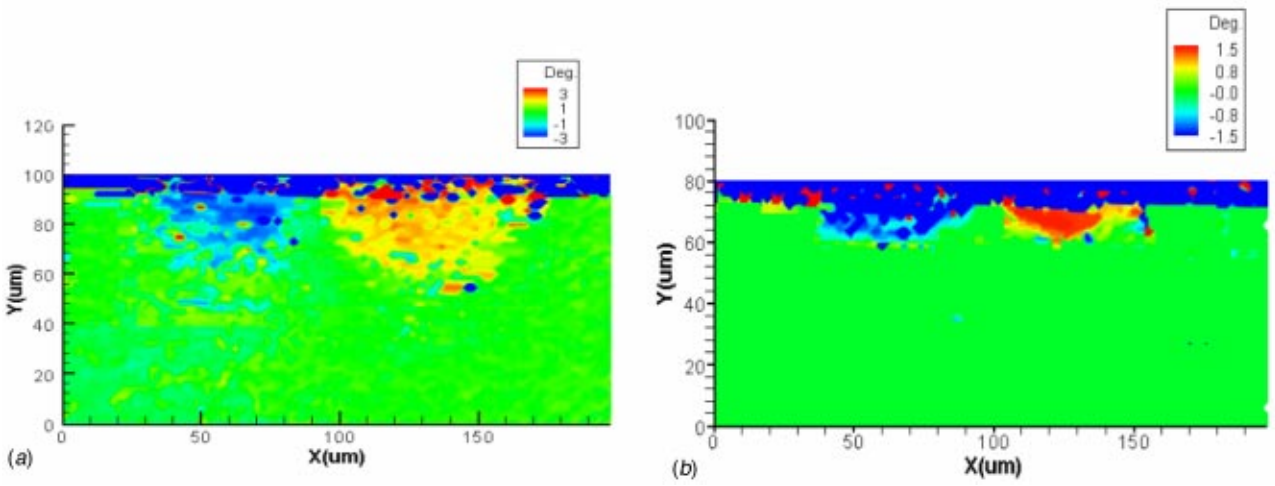

Fig. 7 Lattice rotation contour at the cross section (*a*) Al($1\bar{1}0$) sample; (*b*) Cu($1\bar{1}0$) sample

dimensional deformation state exists. We will appeal to this apparent two-dimensional deformation state when interpreting the other experimental data presented herein.

3.2.2 Lattice Rotation Measurement Results. Lattice rotation measured from top surface across the shocked line. The lattice rotation contour map on the shocked Al($1\bar{1}0$) sample's surface is shown in Fig. 6(*a*). Figure 6(*b*) shows the spatial distribution of lattice rotation along four lines across the shocked line with spacing$=20$ μm. The red region corresponds to counterclockwise rotation about the *Z*-axis which is positive and the blue region corresponds to clockwise rotation which is negative. It is clear to see that the lattice rotation is zero (green region) far away from the shocked line which corresponds to the shock-free region. Again, the lattice rotation distribution along the shocked line is quite uniform which further suggests the approximate two-dimensional deformation state mentioned before. The lattice rotation value is $\pm 3°$ between ± 35 μm from the center of shocked line and the rotation direction is anti-symmetric on both side of shocked line.

Figure 6(*c–d*) shows the lattice orientation change on the shocked Cu($1\bar{1}0$) sample surface. It is clear that both aluminum and copper shows the similar lattice rotation pattern. However, the region for lattice rotation in the copper sample is around ± 20 μm from the center of shocked line and the maximum value is about 1.5°, both of which are smaller than that of Al($1\bar{1}0$) sample.

In order to investigate the effect of crystal orientation on lattice rotation, an aluminum sample shocked on the (001) surface was also studied. Figure 6(*e–f*) shows the lattice rotation contour on the shocked surface. Compared with result of Al($1\bar{1}0$), the general trend of lattice rotation such as the rotation direction and magnitude is the same, but the shocked region is somewhat narrower.

Lattice rotation measured from cross section perpendicular to shocked line. From the measurement mentioned above, we obtained the lattice rotation result on the laser shock peened surface. In order to measure the lattice rotation below the sample surface and study the spatial distribution in the depth direction, the sample was sectioned via wire EDM and the crystallographic orientation of the newly exposed surface was mapped using EBSD. Then the in-plane lattice rotations beneath the laser shocked surface were measured via EBSD. Here we use the term ''in-plane'' because the experimental results indicate an approximate two-dimensional deformation state.

Figure 7(*a*) shows the lattice rotation in the cross section of the Al($1\bar{1}0$) sample. The lattice rotation varies between $\pm 3°$ in the region up to 40 μm below the sample surface. In the center of shocked line, the lattice rotation is nearly zero (green) and rotation direction reversed across the shocked line, which is consistent with the result from sample surface. The maximum lattice rotation occurs near the sample surface and the value decays as depth increases. Figure 7(*b*) shows the lattice rotation of on the cross section for the Cu($1\bar{1}0$) sample. The rotation distribution is similar in character to the Al sample, but the affected region in the depth direction is around 15 μm below the sample surface, smaller than that of Al sample. Also the total rotation angle varies between $\pm 1.5°$, rather than $\pm 3°$.

3.3 Lattice Rotation Measured by X-Ray Microdiffraction Spatially resolved residual stress/strain can be measured on the laser shock peened surface using X-ray microdiffraction from synchrotron radiation sources, [6]. It is also possible to determine lattice orientation on the shocked surface as a byproduct of the X-ray strain/stress measurement.

As discussed in [6] and illustrated in Fig. 8, two rotations, θ scan and χ scan were applied in the experiment by rotating the specimen until the maximum intensity is located in the detector in order to properly align the specimen in the X-ray apparatus. The θ scan ensures that the mean beam vector of incident X-ray, and not any other, is at the proper angle with respect to the surface and consequently, the proper diffraction angle is recorded by the detector arm. The χ scan ensures that the normal vector of the diffracting plane is contained in the same geometrical plane as the incoming and diffracted X-ray beams. These two scans applied

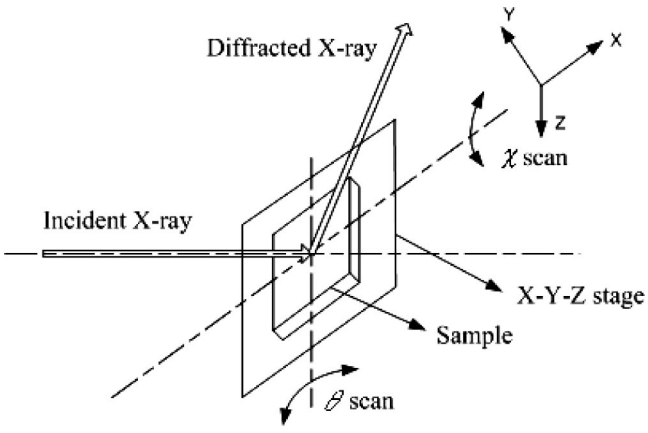

Fig. 8 Scan scheme of X-ray microdiffraction

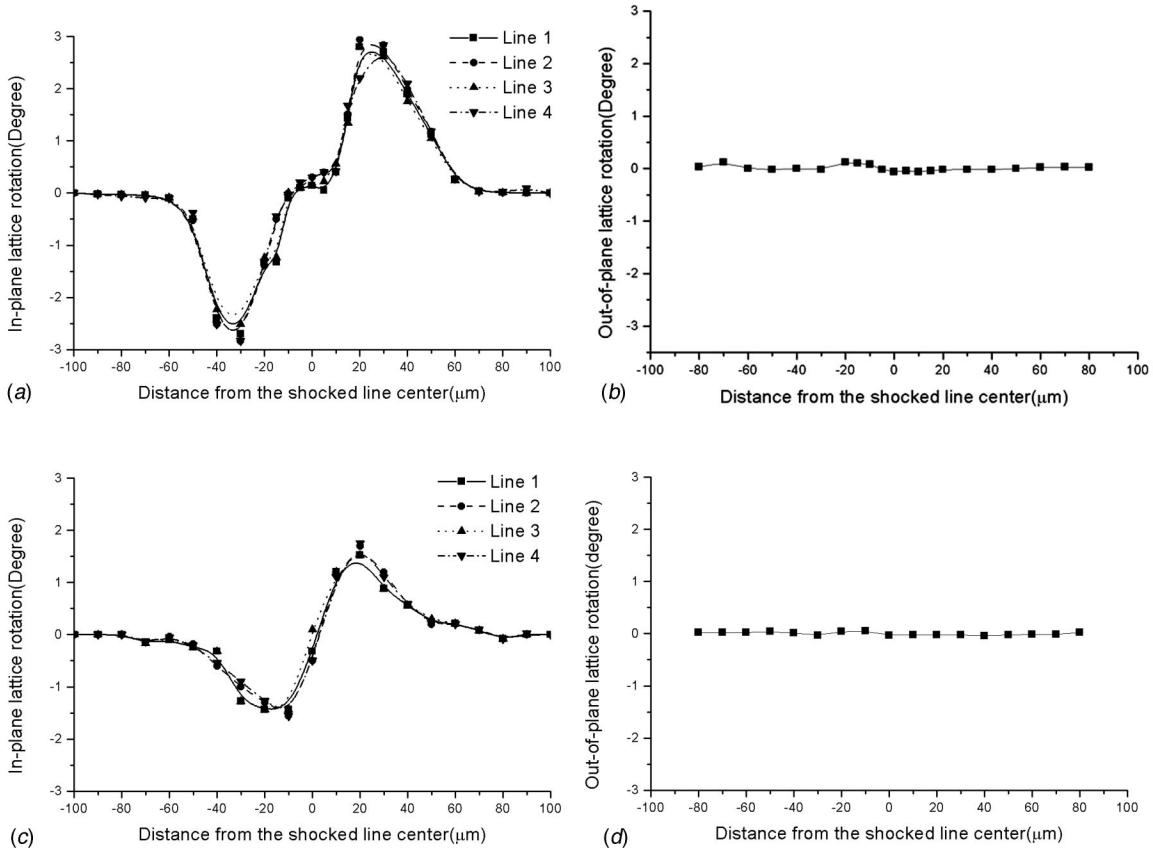

Fig. 9 (*a*) In-plane lattice rotation on shock peened surface of Al($1\bar{1}0$) sample. (*b*) Out-of-plane lattice rotation on shock peened surface of Al($1\bar{1}0$) sample. (*c*) In-plane lattice rotation on shock peened surface of Cu($1\bar{1}0$) sample. (*d*) Out-of-plane lattice rotation on shock peened surface of Cu($1\bar{1}0$) sample.

iteratively optimize the integrated intensity of the relevant reflection during alignment. In essence, the sample is rotated about its Z-axis to perform the θ scan, and about its X-axis to perform the χ scan. Therefore, the in-plane and out-plane lattice rotation can be obtained from the θ and χ scans as shown in Fig. 8.

Results of these measurements in Fig. 9(*a*) indicate that the spatial distribution of in-plane lattice rotation for the Al($1\bar{1}0$) sample is very similar to the EBSD results in Fig. 6(*a*) and 6(*b*). The maximum rotation angle is around $\pm 3°$ at position nearly ± 30 μm away from the center of shock line. While the variation of out-of-plane lattice rotation in Fig. 9(*b*) is only $\pm 0.1°$ which is quite small relative to in-plane lattice rotation. So this measured lattice rotation under shock peening is consistent with the uniform AFM profile along shock direction and two-dimensional in-plane lattice rotation assumption. Figures 9(*c*) and (*d*) shows similar results for Cu($1\bar{1}0$) sample. Thus, the lattice rotation measurements directly complement the material residual strain/stress measurements. Moreover, it also gives an indication of the extent of the plastic deformation induced by the microscale laser shock peening. Lattice rotation measured by X-ray microdiffraction is apparently more uniform than that from EBSD measurement, probably because X-rays penetrate deeper (20–30 μm), [13], than the electron beam used in EBSD (a few microns) and thus average the orientation over a large volume of material. The residual stress measurements that resulted from these experiments are discussed in detail in [6].

4 Theoretical Explanation and Simulations

In this section, we present results of elementary simulations of microscale laser-shock peening. Since the surface deformation and lattice rotation under laser shock peening indicate that an approximate two-dimensional deformation state exists, we will assume that the induced deformation state is strictly two-dimensional, which may be greatly oversimplified. However, it turns out that such an approach can shed significant insight into the mechanics of deformation which will be useful when the full three dimensional problem is addressed in future studies. Simulations of LSP pose many challenges because of the high transient pressures, fluid-solid interaction and high strain rates in a single crystal at the micrometer length scale which raises the possibility of the necessity to account for strain gradient effects. Given the

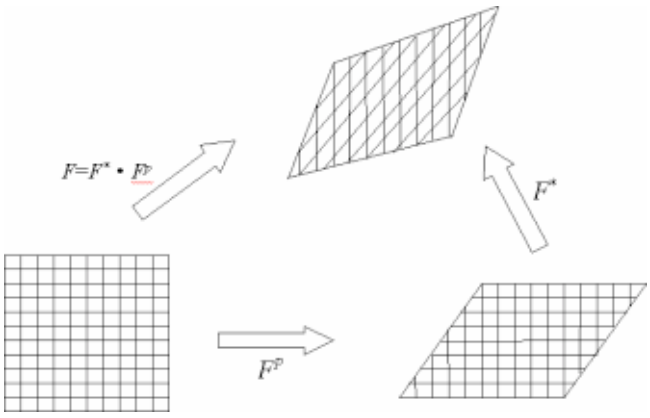

Fig. 10 Plastic deformation in single crystal plasticity

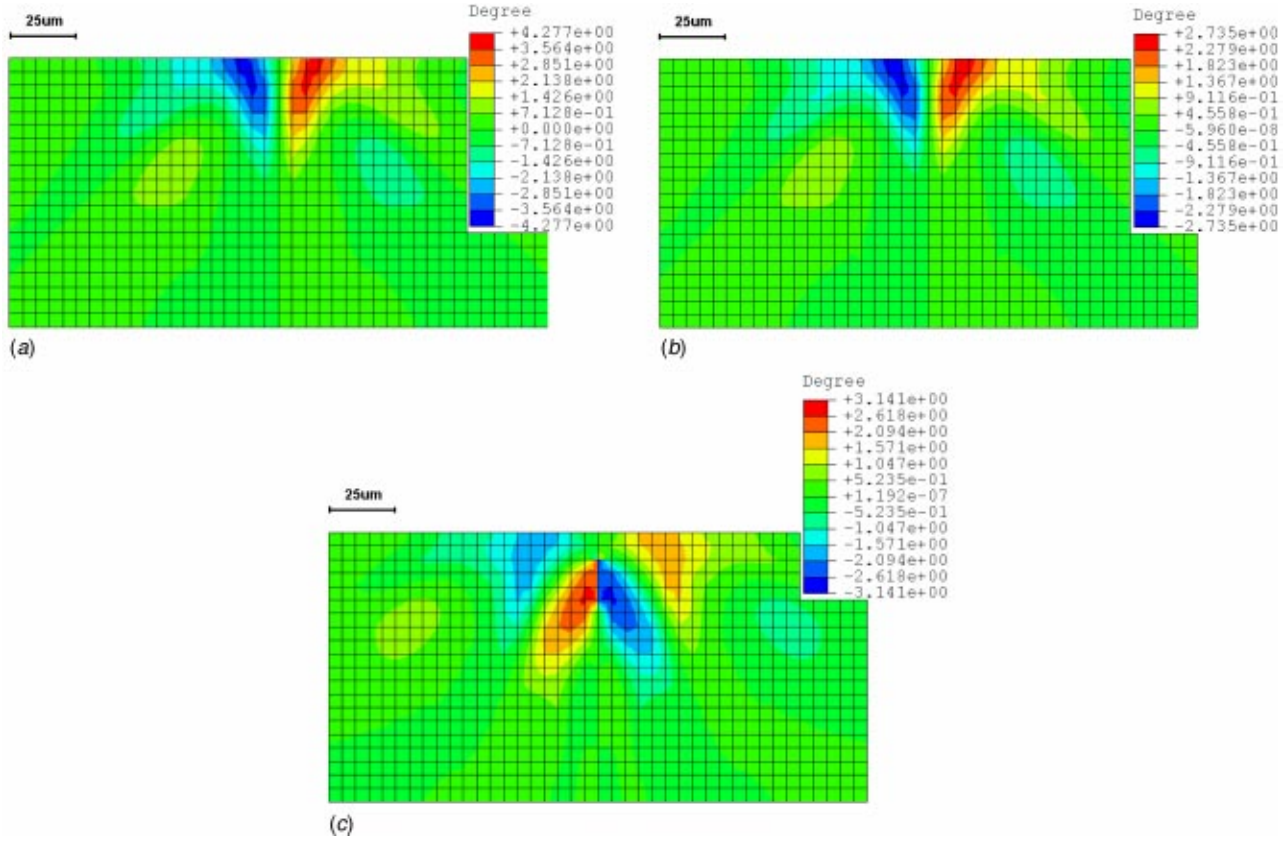

Fig. 11 Lattice rotation field on cross section of after laser shock peening; (*a*) Al$(1\bar{1}0)$, (*b*) Cu$(1\bar{1}0)$, (*c*) Al (001)

absence of constitutive data in this regime, it is impossible to incorporate realistically these effects into the model. Hence, we will make a grossly simplified assumption of ideal plastic behavior under quasi-static plane-strain conditions while implementing single crystal plasticity. Rate effects, hardening, strain gradient, and three-dimensional effects are neglected.

The goal of the simulation is then to attempt to understand the overall character of the deformation and lattice rotation fields and see how much can be predicted by such a simple simulation. In doing so, we can ascertain which of the dominate features of the fields are attributable to the anisotropic plastic behavior of the single crystal. Subsequent simulations, which account for more realistic material constitutive behavior, can then concentrate how the additional effects modify the baseline solution. Thus, this oversimplified approach can shed insight into the mechanics of deformation and lay the ground work for more realistic simulations in future studies which will include three-dimensional, dynamic, and strain-rate effects.

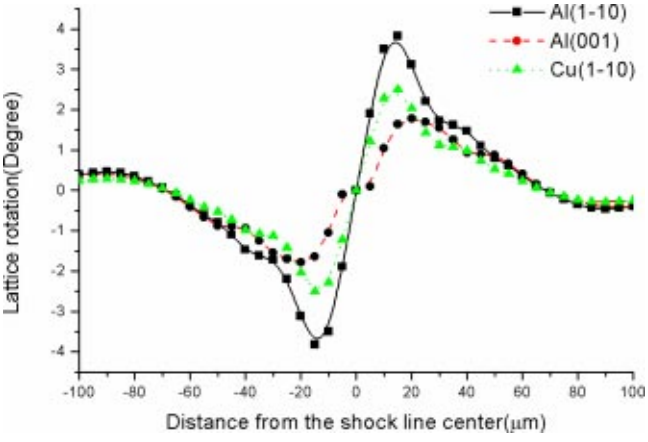

Fig. 12 Spatially distribution of latticed rotation on sample surface from simulation

4.1 Kinematical Theory of Single Crystal Mechanics

From single crystal plasticity theory, [14–16], there are two physically distinct mechanisms for deforming and reorienting materials—plastic slip and elastic lattice deformation. In general, the deformation gradient of a single crystal that undergoes plastic deformation can be written with reference to Fig. 10 as

$$F = F^* \cdot F^P \tag{1}$$

where F^P corresponds to the deformation caused by plastic shearing on crystallographic slip systems and F^* is caused by elastic stretching and rotation of the crystal lattice. The velocity gradient of material is given by a standard formula:

$$L = v\nabla = \dot{F} \cdot F^{-1} = D + \Omega. \tag{2}$$

The D and Ω terms are the symmetric rate of stretching tensor and the antisymmetric rate of spin tensor, respectively. They are then decomposed into parts due to plastic slip (D^P, Ω^P) and lattice deformation (D^*, Ω^*) as follows:

$$D = D^* + D^P, \quad \Omega = \Omega^* + \Omega^P. \tag{3}$$

The lattice rotation measured in the experiment is the Ω^* term integrated throughout the deformation history. The reader interested in the distinction between Ω^* and Ω^P-may refer to pg. 107 of Asaro's review paper, [16], for a full discussion of which rotation components leads to the measured lattice rotation field.

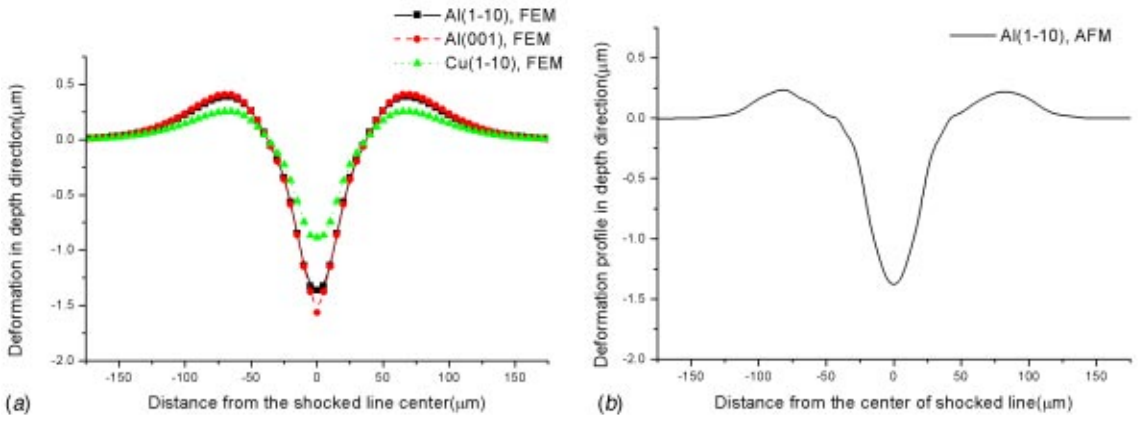

Fig. 13 Deformation profile in depth direction from simulation and AFM; (*a*) FEM result, (*b*) AFM result

4.2 FEM Analysis of Shock Peening With UMAT Incorporating Single Crystal Plasticity. A user-material subroutine (UMAT) for single crystal plasticity based on theory in [16] and written by Huang [17] and modified by Kysar [18] is incorporated into the finite element analysis using the general purpose finite element program ABAQUS/Standard, [19]. In the UMAT, the $\{111\}\langle 110\rangle$ slip systems in FCC metal are used for both single crystal Al and Cu. A critical shear strength $\tau_{\mathrm{CRSS}}=1$ MPa on each of the slip systems is assumed. The simulation is a two-step quasi-static loading and unloading process corresponding to the shock peening and relaxation processes. Following the work of Zhang and Yao [7], shock pressure obeys Gaussian spatial distribution, with its $1/e^2$ radius equals to $\sqrt{2}R$, where R is the radius of plasma. Letting x be the radial distance from the center of the laser beam, the spatially nonuniform shock pressure $P(x)$ is then given as

$$P(x)=P_0\exp\left(-\frac{x^2}{2R^2}\right) \tag{4}$$

on the shocked surface. P_0 is the peak value of shock pressure and the plasma radius $R=10\ \mu$m here. In order to make a dimensionless analysis, all simulation results are normalized as the function of two dimensionless parameters $(P_0/\tau_{\mathrm{CRSS}}, x/R)$. The boundary conditions of the plane strain model are as follows. At the top surface, surface traction equals the applied shock pressure, at the bottom surface, the vertical displacement is specified to be zero and the outer edges are traction-free. In the simulation, elastic-ideally plastic behavior is assumed so that hardening is neglected. In order to eliminate ''volume-locking'' which occurs in plastic deformation simulation, four-node linear elements with reduced

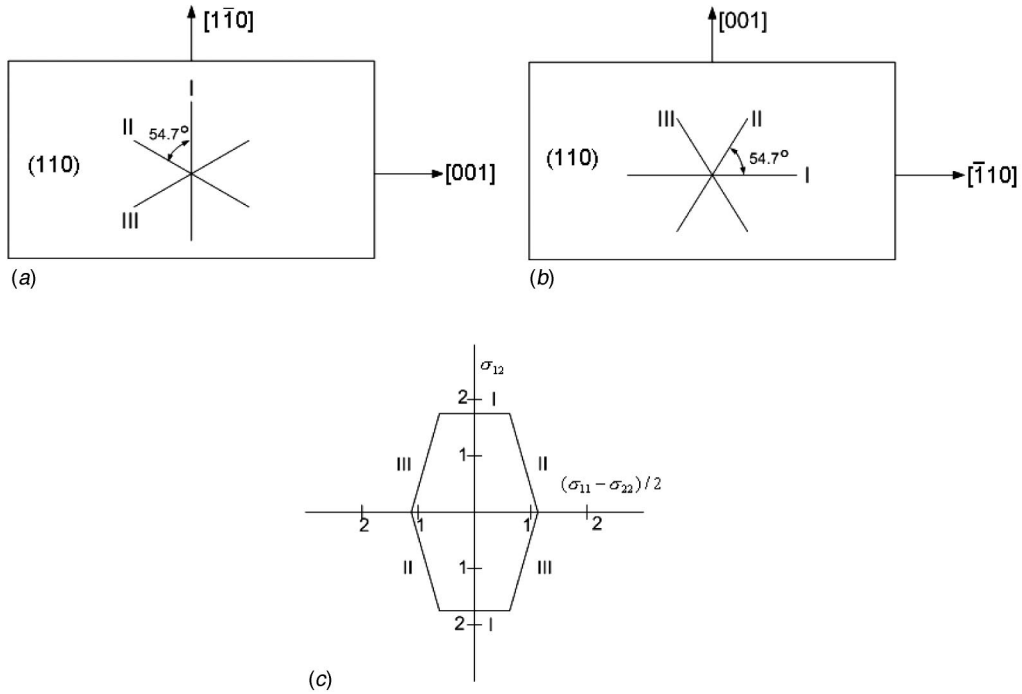

Fig. 14 Three plane-strain slip systems and yield surface in (110) plane; (*a*) Al(1$\bar{1}$0) and Cu(1$\bar{1}$0) sample, (*b*) Al (001) sample, (*c*) yield surface in (110) plane

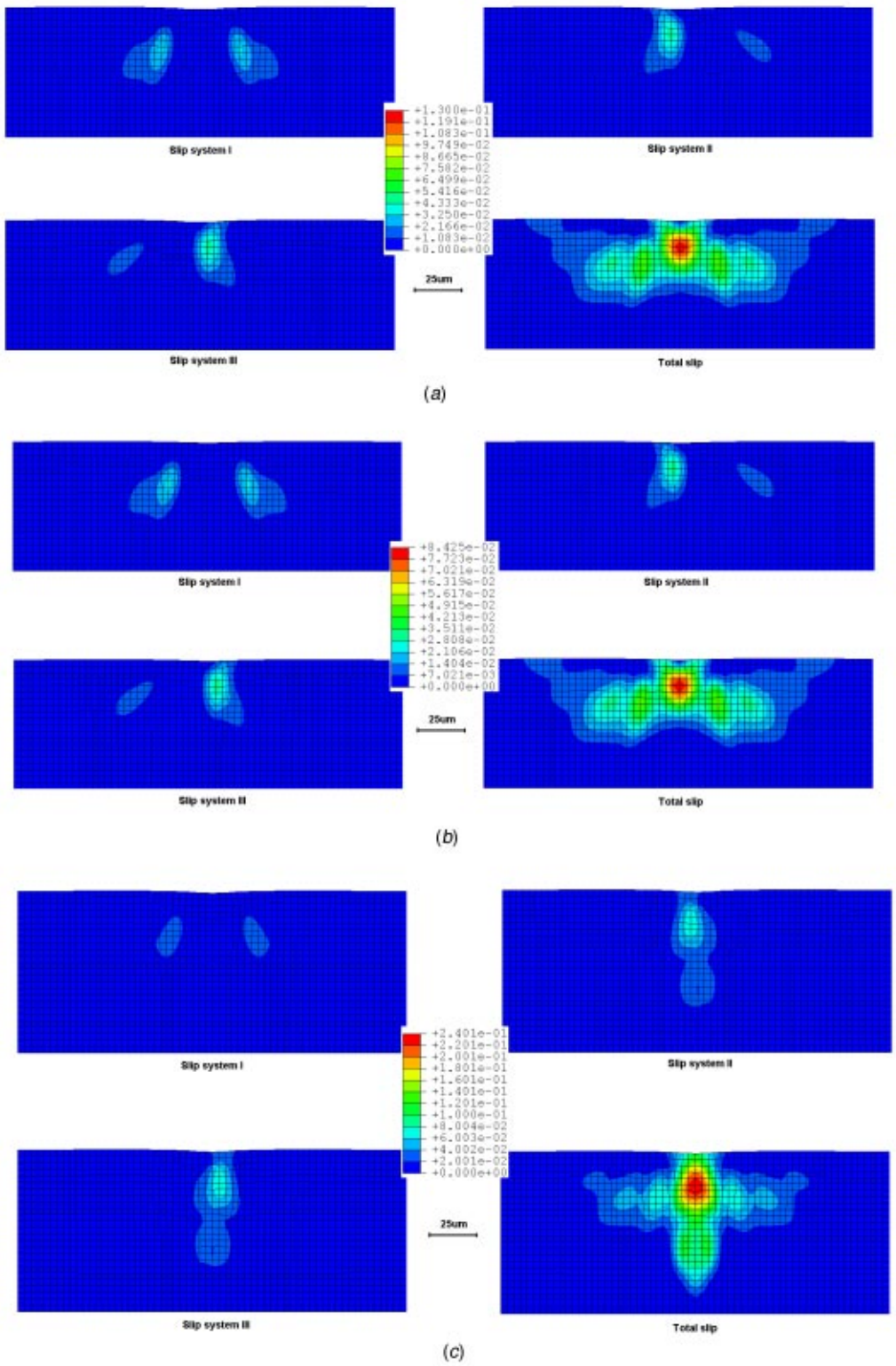

Fig. 15 Shear strain on active slips under laser shock peening from simulation; (*a*) shear strain of active slip systems for Al$(1\bar{1}0)$ sample, (*b*) shear strain of active slip systems for Cu$(1\bar{1}0)$ sample, (*c*) shear strain of active slip systems for Al (001) sample

integration and hourglass stiffness control are used. Two orientations and two materials are simulated, Al$(1\bar{1}0)$, Al (001), and Cu$(1\bar{1}0)$.

4.3 Finite Element Simulation Results. *Lattice rotation field for Al and Cu.* In Fig. 11(*a*), the calculated lattice rotation fields below the laser shocked surface of the Al$(1\bar{1}0)$ sample are shown. The shock pressure loading has been removed in the second step of simulation and the peak value of shock pressure is $P_0/\tau_{CRSS}=7$. The experimental results with the same material and same orientation is shown in Fig. 7(*a*). It can be seen that the antisymmetric pattern of lattice rotation field and the sign of ro-

tation (+, counterclockwise, −, clockwise) is consistent with the experiment result from EBSD (Fig. 7(*a*)). The magnitude of rotation is around $\pm 4°$ in simulation which is close to the $\pm 3°$ from experiment result. The lattice rotation field in the simulation extends over a region across the shock line center with width of $\pm 40\ \mu$m (0 corresponds to center) and depth of 35 μm.

Figure 11(*b*) shows the analogous lattice rotation fields for Cu$(1\bar{1}0)$ sample under laser shock peening and the peak value of shock pressure is $P_0/\tau_{\mathrm{CRSS}}=7$ which is the same as that for Al. For Cu$(1\bar{1}0)$ sample, the lattice rotation field is similar with that of Al except the magnitude of rotation is only 2.7°, less than that of Al (4°). This is consistent with the experimental results from Fig. 7(*b*) and it is mainly due to the larger elastic modulus of Cu.

Figure 11(*c*) shows the lattice rotation field of Al (001) sample from simulation. On the shocked surface, the lattice rotation direction and magnitude is almost the same with that of Al$(1\bar{1}0)$ sample and consistent with the experiment result in Fig. 6(*e–f*). However, the predicted lattice rotation field in the depth direction is significantly different than that of Al$(1\bar{1}0)$ in that the affected region in depth direction is about two times deeper than that of Al$(1\bar{1}0)$ and the magnitude of rotation is $\pm 3°$, less than the $\pm 4°$ of Al$(1\bar{1}0)$. The change in sign of lattice rotation which occurs around 25 μm below the surface does not correspond to the transition from a compressive residual stress state to a tensile residual state, which occurs at approximately 80 μm below the surface.

Figure 12 shows the predicted spatial distribution of lattice rotation on the sample surface for Al$(1\bar{1}0)$, Cu$(1\bar{1}0)$, and Al(001) which can be compared with the experiment result from Fig. 6(*b*), (*d*), and (*f*). The lattice rotation distribution is quite similar to the experimental results. When the position changes from left of shock line to the right, the lattice rotation starts from zero degrees (beyond $\pm 40\ \mu$m) to maximum negative value ($-4°$ at $-15\ \mu$m) and after that, the magnitude of lattice rotation decreases to zero again close to the shocked line center. For the right side of shock line center, the distribution is antisymmetric with the left side.

According to the comparison above, it can be seen that the lattice rotation fields under shock peening depend mainly upon crystal orientation. For the same orientation of FCC material such as Al$(1\bar{1}0)$ and Cu$(1\bar{1}0)$, the lattice rotation fields are quite similar except the magnitude of rotation is less for Cu due to the larger elastic modulus and shear strength. If the orientation is different, even in same material such as Al(001) and Al$(1\bar{1}0)$, the lattice rotation fields on shock peened surface is still similar, however, they are quite different in depth direction below the sample surface.

Figure 13(*a*) and (*b*) compares the indentation profiles induced by laser shock peening between FEM simulation and AFM result for the Al$(1\bar{1}0)$ sample. Figure 13(*b*) shows "composite" surface profile from several AFM measurements across the shocked line. As is expected from the approximately incompressible material behavior, significant pile up around the indentation region (see Fig. 13(*b*)) is observed and agrees well with simulation result. Surface ablation is not observed by either SEM or AFM which is probably due to the protective coating layer on the top of samples.

Slip system and yield surface analysis. The plastic slip systems in a face-centered cubic crystal exhibit mirror symmetry about the (110) plane, so that sustained plastic flow under plane strain conditions in the (110) plane is possible as long as a slip system and its mirror image are activated in equivalent amounts. Thus, there are three pairs of effective slip systems that satisfy these conditions as shown in Fig. 14(*a*) and (*b*), [9]. The yield surface which defines graphically the criterion for plastic slip in a stress space with abscissa $(\sigma_{11}-\sigma_{22})/2$ and ordinate σ_{12}, [8], is shown in Fig. 14(*c*). Plastic slip occurs only when the stress state lies on the yield surface with stress increment directed out of the yield surface.

Figure 15(*a–c*) shows the predicted shear strain on each slip system, as well as the total accumulated slip summed over all slip systems for all three samples. It can be seen that the shear strain is close to zero on the top surface for slip system I in (*a*). Since on sample free surface, $\sigma_{12}=0$, the stress state must lie on the abscissa of the yield surface in Fig. 14(*c*). Therefore, plastic deformation near the surface is caused by slip systems II and III so that the shear strain for slip system I is zero near the free surface and only II and III slip systems are active. For the region around 20 μm below the surface, all three slip systems are active. Shear strain simulation on each slip system is shown in Fig. 15(*b*) for Cu$(1\bar{1}0)$ sample also and the result is quite similar with that of Al$(1\bar{1}0)$, except the magnitude of shear strain is 35% less than that of Al. Figure 15(*c*) shows the same simulation for Al (001) sample; it can be seen that the magnitude of shear strain is almost two times larger than that for Al$(1\bar{1}0)$ and the spatial distribution is different in that the affected region is two times deeper than Al$(1\bar{1}0)$. The shear strain in slip system I is also much smaller than other two slip systems.

5 Conclusions

In this study, new experimental methodologies using EBSD and X-ray microdiffraction are employed which enable measurement of the in-plane lattice rotation component of the deformation gradient under plane-strain conditions. The lattice rotation field under laser shock peening is found to be antisymmetric on and below the shock peened single crystal Al and Cu surface. For the Al$(1\bar{1}0)$ sample, the magnitude of rotation is $\pm 3°$ and covers a region around $\pm 35\ \mu$m across the shock line center on peened surface and reaches 40 μm below the surface. For Cu$(1\bar{1}0)$ sample, the magnitude of rotation is $\pm 1.5°$ and the affected region is $\pm 20\ \mu$m on surface and 15 μm below the sample surface. Single crystal plasticity FEM analysis shows an interesting correspondence between the experimental results and theoretical predictions. Lattice rotation fields are quite similar for Al and Cu with the same $(1\bar{1}0)$ orientation and different for Al with (001) orientation. FEM simulation shows only certain slip systems are active on shock peened surface with more active below the surface. Lattice rotation measurements made as a byproduct of residual strain/stress measurements by X-ray micro-diffraction using synchrotron light source also give an indication of the extent of the plastic deformation induced by the microscale laser shock peening.

The experimental methodology and results presented herein set the stage for further study of the microscale laser shock peening process both experimental and computational. It is now possible to systematically measure the extent and character of crystal lattice rotation fields, as well as to measure the induced residual stresses with micron spatial resolution. Thus it is possible to apply these techniques to determine the optimum laser-shock processing parameters (i.e., laser intensity, time of shock, shock spacing, etc.) which induce the maximum residual stress.

Acknowledgments

This work was supported by the National Science Foundation under grant DMI-02-00334. JWK would like acknowledge support by the National Science Foundation under the Faculty Early Career Development (CAREER) Program with grant CMS-0134226. Guidance in X-ray micro-diffraction provided by Dr. I. Cev Noyan and Dr. Jean Jordan-Sweet is appreciated. Assistance in technique details in sample preparation for EBSD provided by Dr. Yongxue Gang and Mr. J. B. Chou is also acknowledged.

References

[1] Johnson, K. L., 1968, "Deformation of A Plastic Wedge by a Rigid Flat Die Under the Action of a Tangential force," J. Mech. Phys. Solids, **16**, pp. 395–402.

[2] Clauer, A. H., and Holbrook, J. H., 1981, "Effects of Laser Induced Shock Waves on Metals," *Shock Waves and High Strain Phenomena in Metals-Concepts and Applications*, Plenum, New York, pp. 675–702.

[3] Zhang, W., and Yao, Y. L., 2000, ''Improvement of Laser Induced Residual Stress Distributions via Shock Waves,'' *Proc. ICALEO'00, Laser Materials Processing*, Laser Institute of America, Orlando, FL, **89**, pp. E183–192.
[4] Zhang, W., and Yao, Y. L., 2000, ''Microscale Laser Shock Processing of Metallic Components,'' ASME J. Manuf. Sci. Eng., **124**(2), pp. 369–378.
[5] Chen, H. Q., and Yao, Y. L., 2003, ''Modeling Schemes, Transiency, and Strain Measurement for Microscale Laser Shock Processing,'' ASME J. Manuf. Sci. Eng., submitted for publication.
[6] Chen, H. Q., Yao, Y. L., and Kysar, J. W., 2003, ''Spatially Resolved Characterization of Residual Stress Induced by Microscale Laser Shock Peening,'' ASME J. Manuf. Sci. Eng., to appear.
[7] Zhang, W., and Yao, Y. L., 2001, ''Feasibility Study of Inducing Desirable Residual Stress Distribution in Laser Micromachining,'' *Transactions of the North American Manufacturing Research Institution of SME (NAMRC XXIX) 2001*, Society of the Manufacturing Engineers, Dearborn, MI, pp. 413–420.
[8] Rice, J. R., 1987, ''Tensile Crack Tip Fields in Elastic-Ideally Plastic Crystals,'' Mech. Mater., **6**, pp. 317–315.
[9] Kysar, J. W., and Briant, C. L., 2002, ''Crack Tip Deformation Fields in Ductile Single Crystals,'' Acta Mater., **50**, pp. 2367–2380.
[10] Randle, V., 1992, *Microtexture Determination and its Applications*, The Institute of Materials, London.
[11] *HKL Channel 5™ User's Manual*, 2001, HKL Technology, Danbury, CT.
[12] Kocks, U. F., 1998, *Texture and Anisotropy*, Cambridge University Press, Cambridge, pp. 44–100.
[13] Cullity, B. D., 1978, *Elements of X-ray Diffraction*, 2nd Ed., Addison-Wesley, London, pp. 13–20.
[14] Hill, R., 1966, ''Generalized Constitutive Relations For Incremental Deformation of Metals By Multislip,'' J. Mech. Phys. Solids, **14**, pp. 95–102.
[15] Rice, R. J., 1977, ''The Localization of Plastic Deformation,'' *Proceedings of 14th International Congress of Theoretical and Applied Mechanics*, **I**., North-Holland, Amsterdam.
[16] Asaro, R. J., 1983, ''Micromechanics of Crystals and Polycrystals,'' Adv. Appl. Mech., **23**, pp. 1–115.
[17] Huang, Y., 1991, ''A User-Material Subroutine Incorporating Single Crystal Plasticity in the ABAQUS Finite Element Program, Mech Report 178,'' Division of Applied Sciences, Harvard University, Cambridge, MA.
[18] Kysar, J. W., 1997. Addendum to ''A User-Material Subroutine Incorporating Single Crystal Plasticity in the ABAQUS Finite Element Program, Mech Report 178,'' Division of Engineering and Applied Sciences, Harvard University, Cambridge, MA.
[19] ABAQUS/Standard User's Manual, 2002. Version 6.2, Hibbit, Karlsson and Sorensen, Inc., Pawtucket, RI.